Lithium niobate tuning fork-enhanced photoacoustic spectroscopy and light-induced thermoelastic spectroscopy

Runqiu Wang,[1,2] Guowei Han,[3] Ying He,[1] Shunda Qiao,[1] and Yufei Ma[1,2,a]

AFFILIATIONS

[1]National Key Laboratory of Laser Spatial Information, Harbin Institute of Technology, Harbin 150001, China
[2]Zhengzhou Research Institute, Harbin Institute of Technology, Zhengzhou 450008, China
[3]Engineering Research Center for Semiconductor Integrated Technology, Institute of Semiconductors,
 Chinese Academy of Sciences, Beijing 100083, China

[a]Author to whom correspondence should be addressed: mayufei@hit.edu.cn

ABSTRACT

In this paper, the performance of two self-designed lithium niobate tuning forks (LiNTF), round-head and tapered LiNTFs, was systematically explored in lithium niobate-enhanced photoacoustic spectroscopy (LiNPAS) and light-induced thermoelastic spectroscopy (LITES) sensors. Finite element analysis results revealed that the stress and surface charge density of the LiNTFs were higher than those of the standard quartz tuning fork (QTF), owing to the high piezoelectric coefficient and electromechanical coupling coefficient of the $LiNbO_3$. The sensing performance of the two LiNTFs was experimentally evaluated, and acetylene (C_2H_2) was used as the test gas for performance validation. In the C_2H_2–LiNPAS system, the $2f$ signal peak values of the round-head LiNTF and the tapered LiNTF were 3.47 times and 4.29 times higher than those of the standard QTF, respectively. When the average time reached 1000 s, the minimum detection limits (MDLs) of the sensor based on round-head LiNTF and the tapered LiNTF were 723 and 450 ppb, respectively. In the C_2H_2–LITES system, the $2f$ signal peak values of the round-head LiNTF and the tapered LiNTF were found to be 3.79 times and 5.13 times higher than that of the standard QTF. The MDLs of the LITES sensor based on the round-head LiNTF and the tapered LiNTF were determined to be 101 and 52 ppb, respectively.

Published under an exclusive license by AIP Publishing. https://doi.org/10.1063/5.0277336

I. INTRODUCTION

Trace gas detection technology has extensive applications in environmental monitoring, food production, chemical industries, and aerospace exploration.[1–8] Laser spectroscopy technology offers advantages such as rapid measurement speed, high sensitivity, and excellent selectivity.[9–13] Among various laser spectroscopy based gas detection techniques, photoacoustic spectroscopy (PAS) is an effective method with a broad linear dynamic range and nondestructive detection capability.[14–18] However, the acoustic resonant cavity used in PAS features a broad response bandwidth, which renders it extremely vulnerable to acoustic interference from the environment. As a modification of traditional PAS detection technology with the advantages of high sensitivity, strong noise resistance, and real-time monitoring, quartz-enhanced photoacoustic spectroscopy (QEPAS) has attracted significant research attention since its inception, leading to continuous development.[19,20] In QEPAS, a quartz tuning fork (QTF) is employed as a sound wave detector. A modulated laser beam passes through the

gap between the two prongs of the QTF within a gas cell containing the target analyte.[21] The gas molecules absorb laser energy, releasing heat to generate acoustic waves, which drive the two prongs to oscillate in opposite directions. Due to the piezoelectric effect of the quartz crystal, the mechanical deformation produces an electric signal, from which the concentration of the target gas is derived. Since QEPAS is a contact technique, both corrosive and oxidative gases can degrade the QTFs' electrodes, thereby compromising sensor performance. This limitation was resolved in 2018 with the proposal of light-induced thermoelastic spectroscopy (LITES), a non-contact alternative.[22] In LITES, the QTF is isolated from the gas cell.[23,24] Residual laser light irradiates the QTF's surface after passing through gas molecules in the cell, inducing localized thermal expansion and elastic deformation.[25–27] The piezoelectric effect of quartz converts this mechanical deformation into electrical signals for gas detection.[28–31] When analyzing oxidizing or corrosive gases, LITES prevents sensor sensitivity degradation and operational lifetime reduction caused by target gas

corrosion of the QTF. The complementary advantages of LITES (non-contact detection) and QEPAS (compact size) allow each to excel in different application scenarios.[32–37]

The performance of QTF is critical to the detection capability of both QEPAS and LITES sensors. Previous studies have demonstrated various optimization strategies for QTF, including geometric reconfiguration of the structure to enhance the prong displacement through stress distribution optimization and centroid adjustment,[38–43] groove etching on the prong surfaces to strengthen piezoelectric coupling and reduce equivalent resistance,[41] and strategic increase in the QTF's length-to-width ratio to better accommodate overtone detection requirements.[44,45] However, the relatively low piezoelectric coefficient of α-quartz (d_{11}=2.3 pC/N) suggests that replacing it with materials exhibiting higher piezoelectric coefficients could enhance the tuning fork's performance.[46] Lithium niobate (LiNbO₃) exhibits a higher piezoelectric coefficient (28 pC/N, 128° rotated Y-cut) than quartz,[47] enabling greater charge density under unit mechanical stress. Furthermore, the efficiency of energy conversion in the piezoelectric materials, measured by the electromechanical coupling coefficient, is positively correlated with the piezoelectric signal amplitude. Compared to the maximum electromechanical coupling coefficient of 0.3 for quartz, that of LiNbO₃ is as high as 0.68.[48]

Given its high piezoelectric coefficient and electromechanical coupling coefficient, LiNbO₃ has been widely used in sensing applications, including acoustic wave sensors, electro-optical sensors, ferroelectric sensors, and photonic sensors.[49–52] LiNbO₃ tuning fork (LiNTF) has also been investigated for measuring viscosity, density, and other fluid properties,[53,54] as well as for magnetic field detection.[55] Recently, Cantatore et al. explored the possibility of employing a LiNTF as a transducer in a photoacoustic spectroscopy-based gas sensor.[56] Their study showed that the LiNTF prototype's performance is comparable to that of a standard QTF. This limitation might be attributed to three factors: (1) the high resonant frequency results in insufficient energy accumulation time; (2) single-side electrode coating leads to at least 50% charge loss; (3) excessive fork thickness causes reduced surface stress and increased air damping.

This study systematically investigated the performance of two self-designed LiNTF, a round-head LiNTF and a tapered LiNTF, in lithium niobate-enhanced photoacoustic spectroscopy (LiNPAS) and LITES, expanding the application of LiNbO₃ as a detector in laser spectroscopy-based gas sensing. The selection of LiNbO₃ crystal cut orientations was elaborated, followed by a comparative theoretical analysis of the two LiNTF and a standard QTF in the two spectroscopy techniques using the finite element analysis (FEA) method. Subsequently, a LiNPAS system and a LITES system were constructed to compare their detection performance in detail. Acetylene (C₂H₂) was used as the test gas for performance validation due to its important application in industrial manufacturing, mining operations, and petroleum gas industries.

II. LINTF SIMULATION

LiNbO₃ is a trigonal crystal system compound belonging to point group 3m and space group R3c, showing threefold rotation symmetry along the c-axis (the spontaneous polarization direction). The accepted conventional coordinate system used to describe the physical tensor properties is a Cartesian system $\{X_{cr}, Y_{cr}, Z_{cr}\}$ where the Z_{cr}-axis is parallel to the crystallographic c-axis, and the X_{cr}-axis is parallel to the a-axis. Crystal orientation is an important consideration in the LiNTF

design. The 128° rotated Y-cut LiNbO₃ was selected for this study due to its good sensitivity in surface acoustic wave applications and commercial availability with cost-effectiveness. It is obtained by rotating the Y-cut LiNbO₃ 128° counterclockwise about the X_{cr}, and $\{X_{cr}, Y_{cr}, Z_{cr}\}$ is also rotated 128° counterclockwise about the X_{cr}-axis to obtain the global coordinate system $\{X_g, Y_g, Z_g\}$, as depicted in Fig. 1(a). As shown in Fig. 1(b), the t-axis (thickness), l-axis (longitudinal), and w-axis (lateral) of the LiNTF align with the Y_g-axis, Z_g-axis, and X_g-axis, respectively. In the simulation, the crystal orientation is typically defined in a rotated coordinate system, with Euler angles used to parameterize the rotational transformation from the global coordinate system $\{X_g, Y_g, Z_g\}$ to the crystal coordinate system $\{X_{cr}, Y_{cr}, Z_{cr}\}$. For the selected 128° rotated Y-cut orientation in this study, the Euler angle is (0°, −128°, 0°).

Adopting the geometric configurations of the previously designed round-head QTF and tapered QTF, the LiNbO₃ counterparts are theoretically compared with the standard QTF through the FEA method. In tuning fork-based PAS (QEPAS and LiNPAS), physical fields including electrostatics, solid mechanics, and pressure acoustics are used to set up the model. To excite the in-plane anti-symmetric flexural mode of the tuning fork, a linear acoustic source that passes through the prong gap is implemented to emulate the acoustic waves generated by the periodic thermal expansion of gas molecules under laser modulation. The linear acoustic source is laterally positioned at the centroid between the two prongs. The eigenfrequency study reveals the fundamental frequency f_0 of 32 142 Hz (standard QTF), 8934 Hz (rounded-head LiNTF), and 8941 Hz (tapered LiNTF). For the standard QTF and round-head LiNTF, the stress is concentrated at the root of the prongs' medial surface, while for the tapered LiNTF, the stress distribution is observed not only at the root but also at the junction of the two trapezoids, as depicted in Figs. 2(a) and 2(c). The maximum stress of the tapered LiNTF is higher than that of the round-head LiNTF, and both of them are greater than that of the standard QTF. The surface charge distributions of the standard QTF and the two LiNTFs are different due to material and cut-type differences. As shown in Fig. 3(a) and 3(c), for the standard QTF, each of the four faces on a single prong carries a single charge type, where adjacent faces exhibit opposite charges and opposing faces share identical charges. The paired prong shows inverted charge configurations on all corresponding faces. However, for the LiNTFs, both prongs have the same charge distributions, primarily concentrated on the front and back faces. Each face of one prong has both positive and negative charges, while the opposing face displays an inverted charge
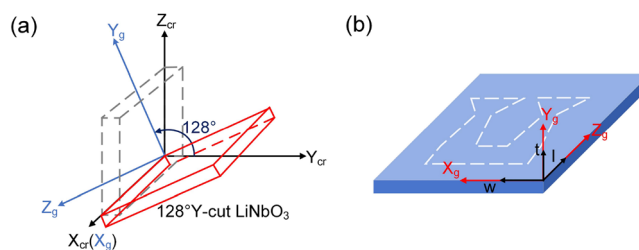

FIG. 1. (a) Schematic diagram of the crystal coordinate system $\{X_{cr}, Y_{cr}, Z_{cr}\}$ and the global coordinate system $\{X_g, Y_g, Z_g\}$ of the 128° rotated Y-cut LiNbO₃ wafer. (b) Schematic diagram of the relationship between the global coordinate axes and the plate axes.
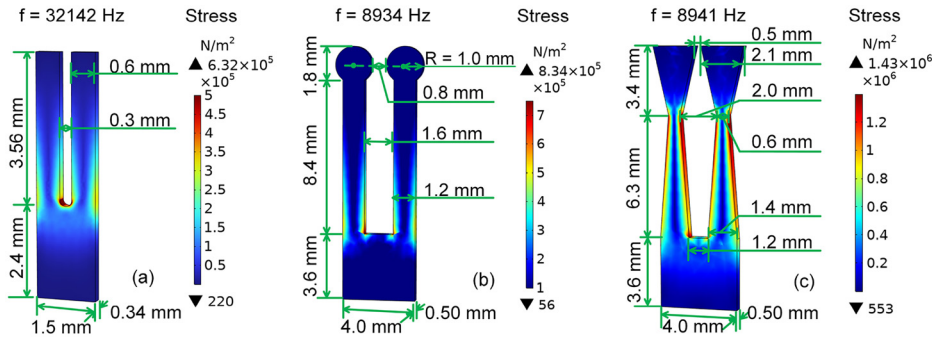
FIG. 2. The geometric parameters and simulation of stress distribution in tuning fork-based PAS: (a) standard QTF, (b) round-head LiNTF, and (c) tapered LiNTF.
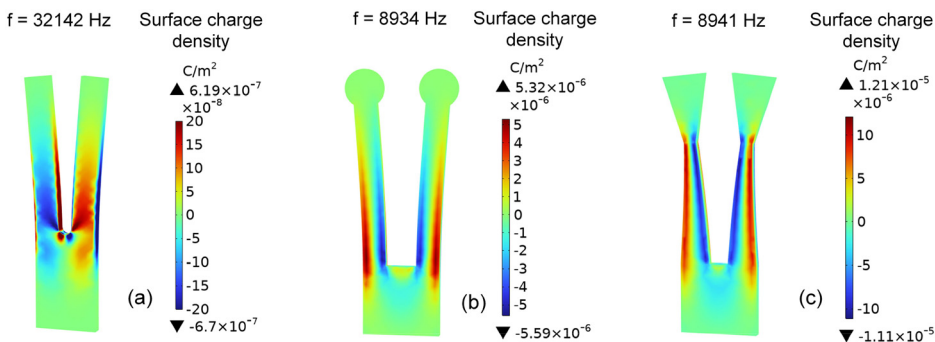

FIG. 3. Surface charge density distribution simulation for PAS systems based on tuning forks: (a) standard QTF, (b) round-head LiNTF, and (c) tapered LiNTF.
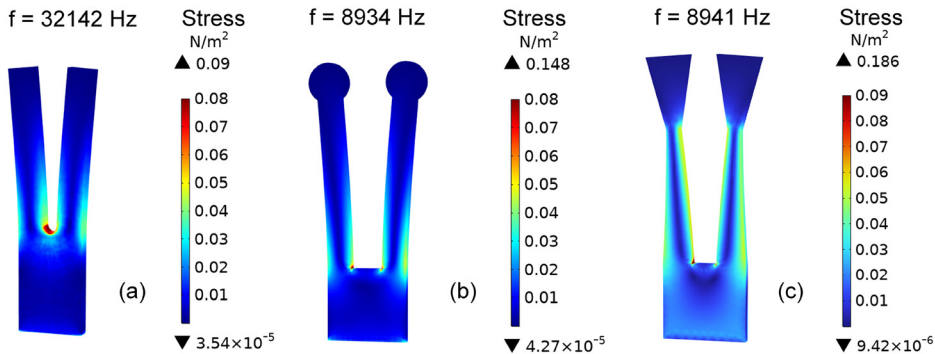

FIG. 4. Stress distribution simulation for LITES technology: (a) standard QTF, (b) round-head LiNTF, and (c) tapered LiNTF.
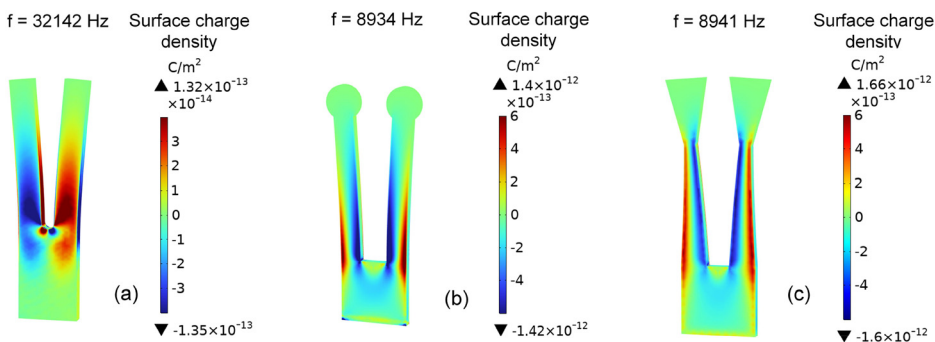

FIG. 5. Surface charge density distribution simulation for LITES systems: (a) standard QTF, (b) round-head LiNTF, and (c) tapered LiNTF.
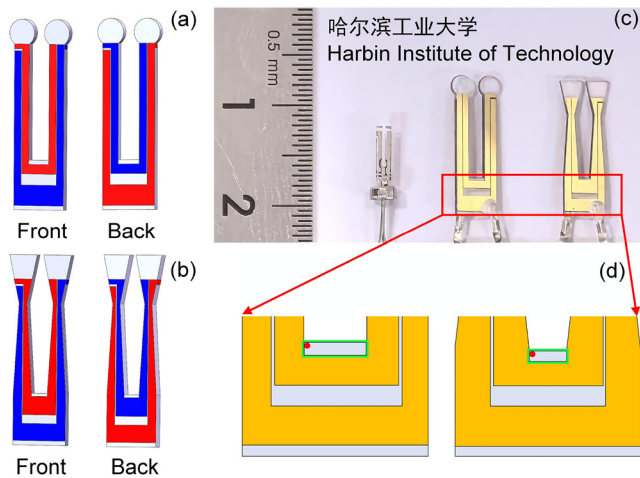
FIG. 6. The electrode pattern schematic of LiNTFs, where the red regions indicate positive charge, and the blue regions represent negative charge: (a) the round-head LiNTF, (b) the tapered LiNTF. (c) Photographs of the standard QTF (left), the round-head LiNTF (middle), and the tapered LiNTF (right). (d) The active area (in green rectangular frame) of the round-head LiNTF and the tapered LiNTF.

FIG. 8. Frequency response of the standard QTF, the round-head LiNTF, and the tapered LiNTF.

distribution pattern. The surface charge densities of the standard QTF, the round-head LiNTF, and the tapered LiNTF increase in sequence.

In the LITES technology, physical fields including electrostatics, solid mechanics, and heat transfer in solids are used to set up the model. A point heat source located at the root of the prong surface, with its power sinusoidally modulated at the resonant frequency of the tuning fork, was used to simulate the laser irradiation on it. This setup induced in-plane symmetric vibration of the tuning fork, as illustrated in Figs. 4(a) and 4(c). The maximum stress of both the round-head
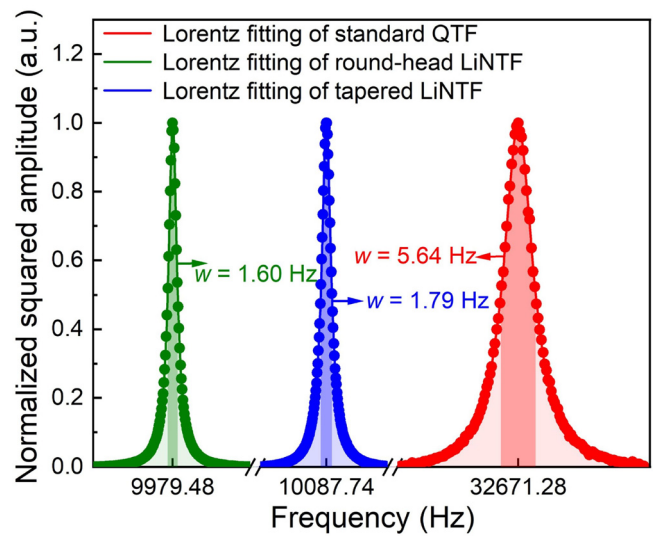
LiNTF and the tapered LiNTF is higher than that of the standard QTF, with the stress of the tapered LiNTF being more significant than that of the round-head LiNTF. The surface charge distributions in LITES are the same as in QEPAS and LiNPAS. As shown in Figs. 5(a) and 5(c), the maximum surface charge density of the standard QTF is lower than that of both the round-head and tapered LiNTFs, with the tapered LiNTF having a higher density than the round-head one. Based on the charge distribution characteristics of the two LiNTFs in LiNPAS and LITES, their charge patterns were designed as illustrated in Figs. 6(a) and 6(b), with red and blue indicating regions of opposite
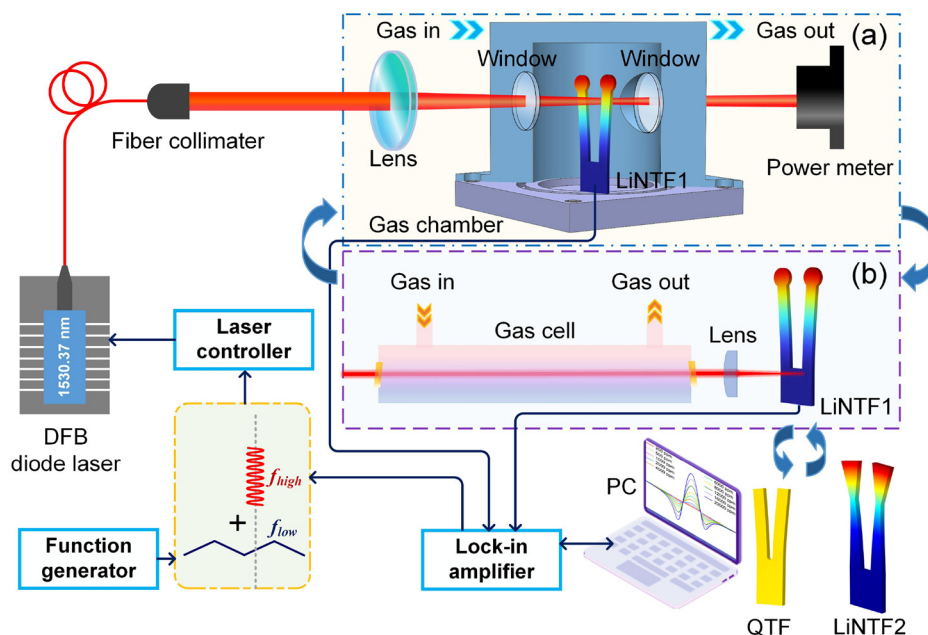

FIG. 7. Schematic diagram of the experimental setup: (a) the experimental setup of the tuning fork-based PAS system (LiNPAS and QEPAS); (b) the experimental setup of the LITES system. DFB diode laser: distributed feedback diode laser, LiNTF: lithium niobate tuning fork, QTF: quartz tuning fork, PC: personal computer.
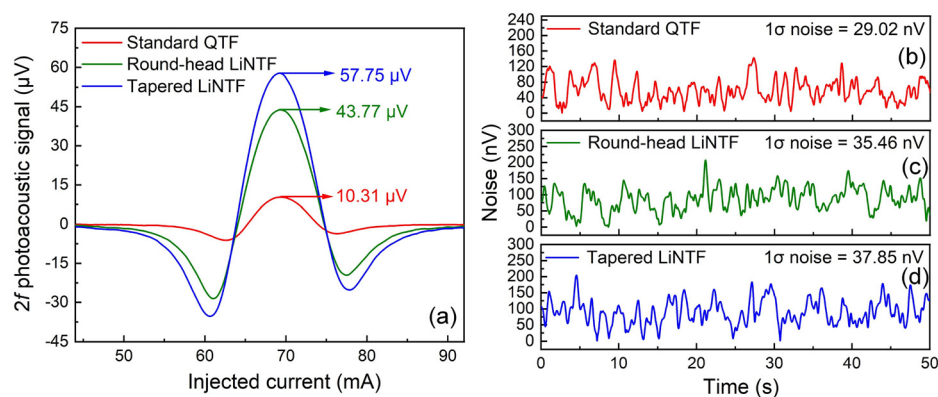
18 October 2025 14:48:07

FIG. 9. (a) $2f$ PAS signals recorded with the standard QTF, the round-head LiNTF, and the tapered LiNTF; the noise of (b) the standard QTF, (c) the round-head LiNTF, and (d) the tapered LiNTF.

charges. In Fig. 6(d), the red dot indicates the laser incidence position, and the green rectangular frame indicates the LITES active areas of the LiNTF. The active areas of the round-head LiNTF and the tapered LiNTF are 0.48 and 0.24 mm^2, respectively.

III. EXPERIMENTAL SETUP

Figure 7(a) illustrates the schematic of the C_2H_2 detection system based on LiNPAS. For performance comparison, three different types of tuning forks were swapped in the system, including the standard QTF, the round-head LiNTF, and the tapered LiNTF. All other hardware components were kept in their original states during the process. To target the specific absorption line of C_2H_2 at approximately

6534.36 cm^{-1}, a single-mode distributed feedback (DFB) diode laser was selected as the excitation light source. This laser operated at an output wavelength of 1.53 μm. To suppress unwanted background signals, a combination of wavelength modulation spectroscopy (WMS) and second-harmonic ($2f$) detection was implemented. The wavelength of the DFB laser was modulated by superimposing a low-frequency sawtooth signal and a high-frequency sinusoidal wave. The low-frequency sawtooth signal was generated by a function generator, while the high-frequency sinusoidal wave was delivered by a lock-in amplifier. The lock-in amplifier was configured with a third-order filter roll-off, and its detection bandwidth was set to 405.5 mHz. The laser beam was collimated and then passed through a wedged window
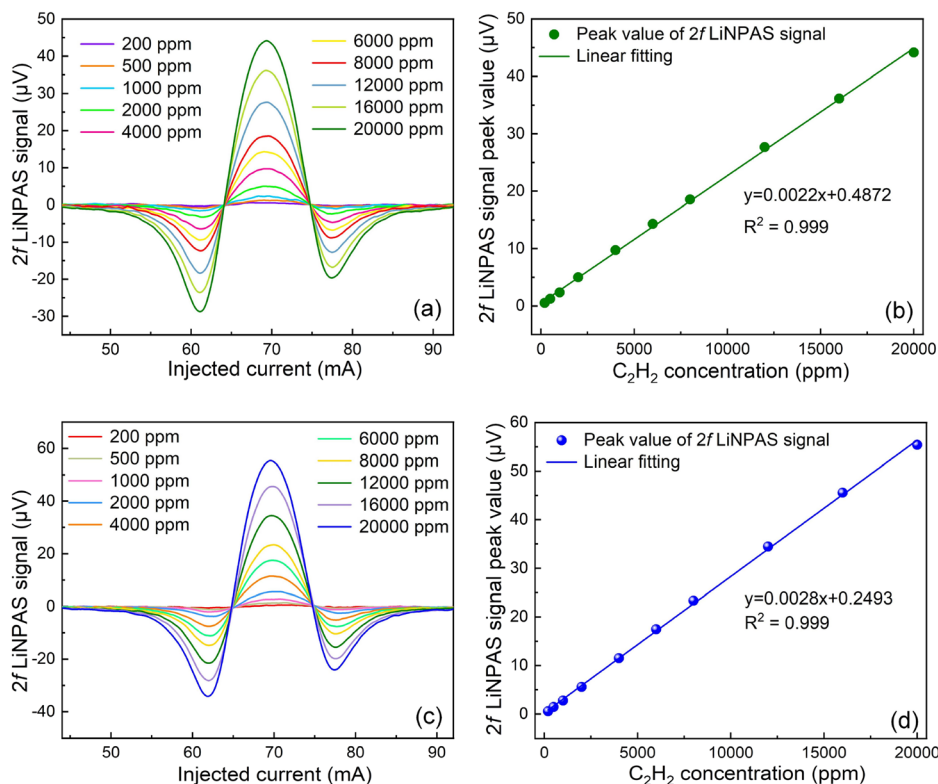

FIG. 10. Concentration response of the C_2H_2–LiNPAS system with two types of LiNTFs: (a) $2f$ signals of the round-head LiNTF at various concentrations; (b) linear correlation between $2f$ signal peak and C_2H_2 concentration; (c) $2f$ signals of the tapered LiNTF at various concentrations; and (d) linear correlation between $2f$ signal peak and C_2H_2 concentration.
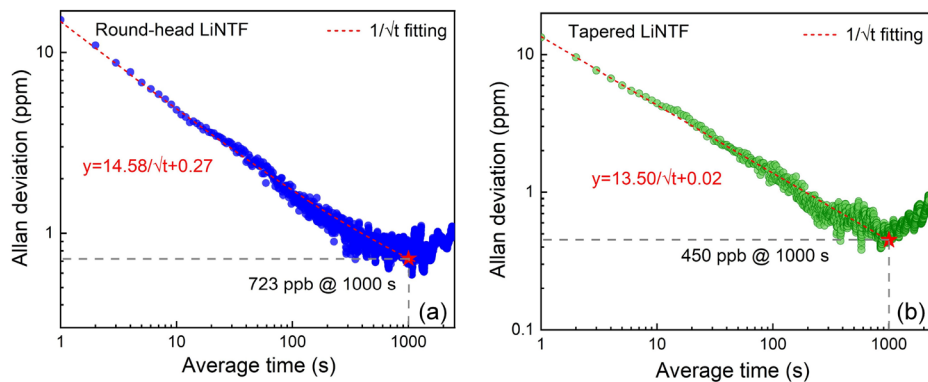
FIG. 11. The Allan deviation analysis of the C_2H_2–LiNPAS system based on (a) the round-head LiNTF and (b) the tapered LiNTF.

into a gas cell, which contained the C_2H_2 sample gas. The structural design of the C_2H_2 detection system based on LITES is shown in Fig. 7(b). In this setup, the collimated laser beam first traversed a gas chamber. This gas chamber has an optical path length of 20 cm. Subsequently, the laser beam was focused onto the root region of the LiNTF using a lens that has a 50 mm focal length.

IV. EXPERIMENTAL RESULTS AND DISCUSSION
A. Performance validation of the LiNTFs in the LiNPAS sensor

First, the resonant frequencies (f_0) of the standard QTF, the round-head LiNTF, and the tapered LiNTF were measured using the optical excitation method. As shown in Fig. 8, the measured values were 32 671.28, 9979.48, and 10 087.74 Hz, respectively. The frequency discrepancies between simulation and experimental results primarily arise from: (i) gas damping, (ii) neglected electrode mass loading in simulations, (iii) mesh/boundary condition idealizations, and (iv) mechanical perturbations induced by the welded base. Following Lorentz fitting to extract their full widths at half maximum (FWHM, w), the corresponding Q factors are determined as 5793, 6237, and 5636, respectively, based on the equation $Q = f_0/w$. Compared to the standard QTF, the LiNTFs exhibit lower f_0 and w, which are advantageous for energy accumulation of the signal. Under the condition of 20 000 ppm C_2H_2 gas, the $2f$ signals were measured and are presented in Fig. 9(a). The peak values of $2f$-LiNPAS based on the round-head LiNTF and the tapered LiNTF are 43.77 and 57.75 μV, respectively, which are 4.25 times and 5.60 times higher than those of the standard

QTF. The noise levels of the tuning forks were measured in pure nitrogen (N_2), with the flowing rate maintained the same as the flowing rate of 20 000 ppm C_2H_2. The noise levels of the round-head LiNTF and the tapered LiNTF are only slightly higher than those of the standard QTF, as shown in Figs. 9(b) and 9(d), with measured values of 29.02, 35.46, and 37.85 nV, respectively, for the standard QTF, the round-head LiNTF, and the tapered LiNTF. Their signal-to-noise ratios (SNRs) are calculated to be 355.27, 1234.35, and 1525.76, respectively, thereby indicating the minimum detection limits (MDLs) to be 56.29, 16.20, and 13.11 ppm, respectively. In the C_2H_2–LiNPAS system, the round-head LiNTF and the tapered LiNTF achieved SNRs 3.47 times and 4.29 times higher than those of the standard QTF, respectively.

Based on the excellent performance of the LiNTFs, they were used in subsequent experiments for further research. The concentration response characteristics were investigated. The $2f$ signals of the round-head LiNTF were measured at different C_2H_2 concentrations ranging from 200 to 20 000 ppm, and the results are shown in Fig. 10(a). Figure 10(b) illustrates the relationship between the $2f$ signal peak value and C_2H_2 concentration, with an R^2 value of 0.999, indicating an excellent linear concentration response of the round-head LiNTF-based LiNPAS sensor. Similarly, Fig. 10(c) presents the $2f$ signals of the tapered LiNTF across the same concentration range. Figure 10(d) shows the relationship between the $2f$ signal peak value and C_2H_2 concentration. With an R^2 value of 0.999, the tapered LiNTF-based LiNPAS sensor exhibits good linearity in concentration response.
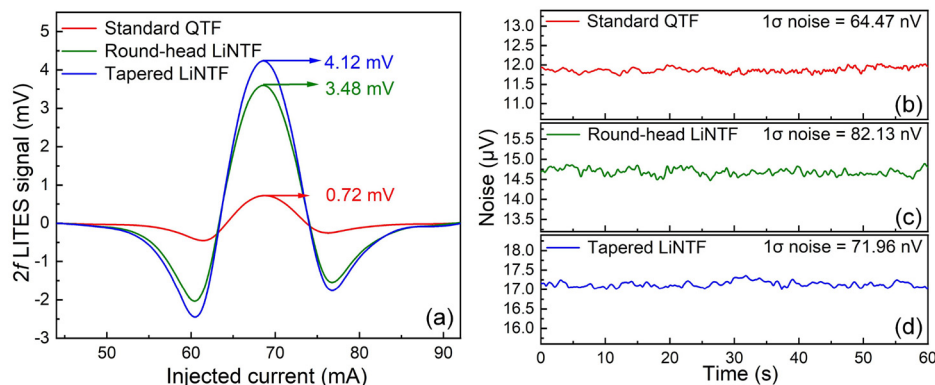

FIG. 12. (a) $2f$ LITES signals recorded with the standard QTF, the round-head LiNTF, and the tapered LiNTF; the noise of (b) the standard QTF, (c) the round-head LiNTF, and (d) the tapered LiNTF.
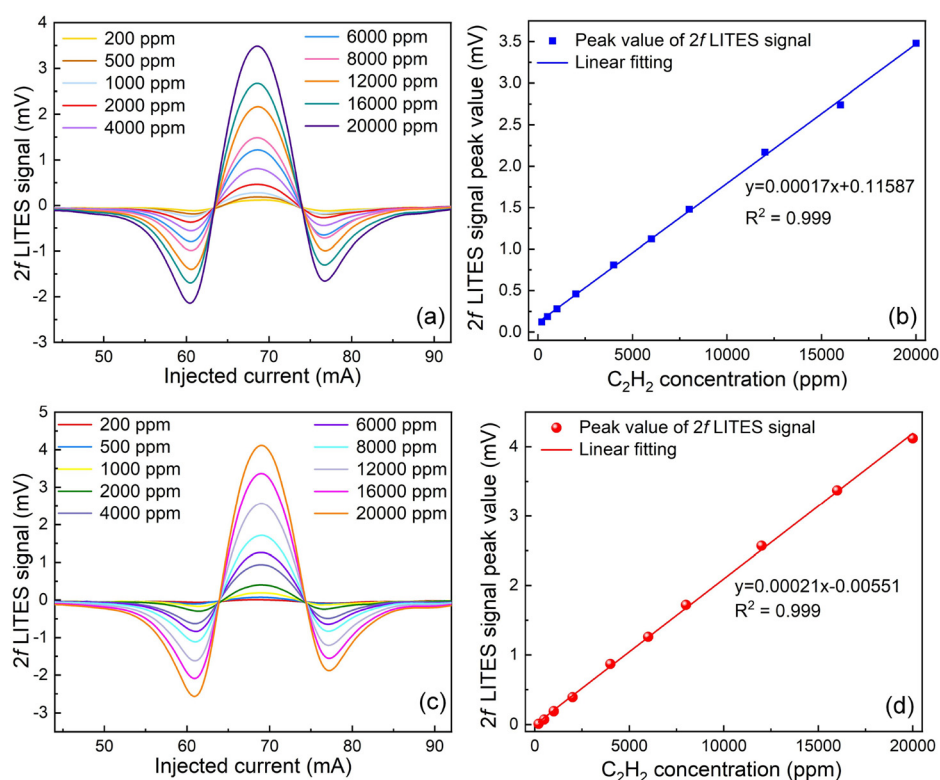
FIG. 13. Concentration response of the C_2H_2–LITES system with two types of LiNTFs: (a) $2f$ signals of the round-head LiNTF at various concentrations; (b) linear correlation between $2f$ signal peak and C_2H_2 concentration; (c) $2f$ signals of the tapered LiNTF at various concentrations; and (d) linear correlation between $2f$ signal peak and C_2H_2 concentration.

Finally, to confirm the long-term stability of the C_2H_2–LiNPAS sensor, the gas cell was filled with pure N_2, and a continuous test was conducted for 2.5 h with a 200 ms time constant. Results from the Allan deviation analysis are presented in Figs. 11(a) and 11(b). As observed, when the system's average time reaches 1000 s, the MDL of the sensor based on the round-head LiNTF is 723 ppb, whereas the MDL of the sensor using the tapered LiNTF is enhanced to 450 ppb.

B. Performance validation of the LiNTFs in the LITES sensor

To further verify the detection performance of the LiNTFs, the C_2H_2–LITES system was built as shown in Fig. 7(b). In LITES, local

thermal expansion results in thermoelastic deformation and vibration. Under the same laser irradiation, the temperature change ΔT is inversely proportional to the product of density ρ and constant-pressure heat capacity C_p. $LiNbO_3$ has a ρ of 4700 kg/m^3 and a C_p of 650 J/(kg K), while quartz has a ρ of 2650 kg/m^3 and a C_p of 730 J/(kg K). Therefore, the temperature change of the QTF will be higher than that of the LiNTFs. Although the temperature change ΔT in the tapered LiNTF is nearly one order of magnitude smaller than that in the standard QTF, the piezoelectric charge density D of LiNTF remains higher. This is because $LiNbO_3$ exhibits an order of magnitude higher thermal expansion coefficient α and piezoelectric coefficient d, as well as a higher Young's modulus E, compared to quartz. Considering the relationship $D = \alpha d \Delta T E$, the combined enhancement factors from α, d, and E
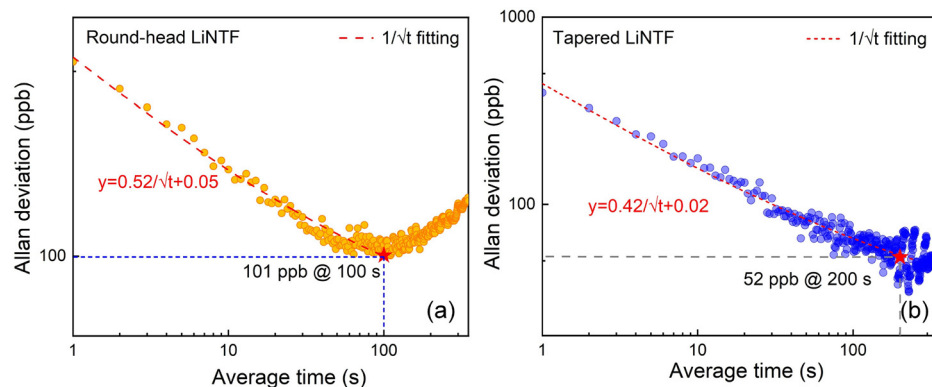

FIG. 14. The Allan deviation analysis of the C_2H_2–LITES system based on (a) the round-head LiNTF and (b) the tapered LiNTF.

TABLE I. Comparison of the performance of the QTFs and LiNTFs with similar geometries.

Method	Detector	Wavelength (nm)	SNR improvement factor	NNEA (W/cm Hz$^{1/2}$)	Reference
QEPAS/LiNPAS	Tapered QTF	1530.37	3.02	1.03×10^{-6}	40
	Tapered LiNTF	1530.37	4.29	3.62×10^{-7}	This work
	Round-head QTF	1650.96	3.26	4.71×10^{-6}	42
	Round-head LiNTF	1530.37	3.47	4.47×10^{-7}	This work
LITES	Tapered QTF	1530.37	3.60	2.25×10^{-8}	40
	Tapered LiNTF	1530.37	5.13	9.65×10^{-9}	This work
	Round-head QTF	1576.29	3.36	$\cdots$	4
	Round-head LiNTF	1530.37	3.79	1.29×10^{-8}	This work

outweigh the reduction in ΔT, leading to a net increase in D for the LiNTF. This result is manifested as higher $2f$ signal peak values of the LiNTFs compared to the standard QTF in Fig. 12(a). At a C_2H_2 concentration of 20 000 ppm, the peak values of $2f$-LITES based on the round-head LiNTF and the tapered LiNTF are 3.48 and 4.12 mV, respectively, which are 4.83 times and 5.72 times higher than that of the standard QTF. The noise levels of the standard QTF, the round-head LiNTF, and the tapered LiNTF were measured to be 64.47 nV, 82.13 nV, and 71.96 nV, respectively, as shown in Fig. 12(b). Their SNRs are 11 167.99, 42 371.85, and 57 254.03, corresponding to MDLs of 1.79, 0.47, and 0.35 ppm, respectively. In the C_2H_2–LITES system, the SNRs of the round-head LiNTF and the tapered LiNTF were 3.79-fold and 5.13-fold higher than those of the standard QTFs, respectively.

The concentration response characteristics of the LiNTF-based LITES sensor were investigated. As shown in Fig. 13(a), the $2f$ signals of the round-head LiNTF were measured at different C_2H_2 concentrations ranging from 200 to 20 000 ppm. Figure 13(b) shows the linear relationship between the $2f$ signal peak value and C_2H_2 concentration for the round-head LiNTF-based LITES sensor, with an excellent R^2 of 0.999. Similarly, Fig. 13(c) presents the $2f$ signals of the tapered LiNTF over the same concentration range, while Fig. 13(d) demonstrates its corresponding superior linear response ($R^2 = 0.999$).

The long-term stability of the two LiNTFs was studied through an Allan deviation analysis. The results were obtained from 2.5 h of detection with a time constant of 200 ms, as shown in Figs. 14(a) and 14(b). The noise level of the round-head LiNTF decreased as the average time increased to 100 s, following the trend of $1/\sqrt{t}$, yielding the MDL of 101 ppb. The Allan deviation signal of the tapered LiNTF reaches an inflection point at 200 s, corresponding to an MDL of 52 ppb.

To demonstrate the advantages of $LiNbO_3$ over quartz as a tuning fork material, Table I summarizes the performance improvement multiples achieved with round-head and tapered QTFs and LiNTFs relative to the standard QTF. Furthermore, to facilitate a direct comparison between systems using LiNTFs and QTFs independent of factors such as target gas species, laser power, or filter bandwidths, the normalized noise equivalent absorption (NNEA) coefficients are also provided. Comparative analysis reveals that LiNTFs consistently achieve a higher SNR compared to geometrically equivalent QTFs across both LITES and LiNPAS systems. However, the manufacturing and design methodologies for LiNTFs remain at an early stage. Further improvements in sensing performance can be achieved by advancing the crystal quality and processing techniques of $LiNbO_3$.

V. CONCLUSIONS

In this paper, we systematically explored the performance of the self-designed round-head LiNTF and tapered LiNTF in LiNPAS and LITES sensors. With a higher piezoelectric coefficient and electromechanical coupling coefficient, the LiNTFs demonstrated a significant advantage over the standard QTFs in piezoelectric signal generation. The simulation results indicated that the stress and the surface charge density of the LiNTFs were higher than those of the standard QTF. The sensing performance of the C_2H_2–LiPAS system and the C_2H_2–LITES system employing the round-head LiNTF and tapered LiNTF was experimentally investigated. For the C_2H_2–LiNPAS systems, the $2f$ signal peak values of the round-head LiNTF and the tapered LiNTF were 4.25 times and 5.60 times higher than that of the standard QTF. The MDLs were 723 and 450 ppb for the round-head LiNTF and tapered LiNTF-based sensors, respectively, when the average time reached 1000 s. For the C_2H_2–LITES systems, the $2f$ signal peak values of the round-head LiNTF and the tapered LiNTF were 4.83 times and 5.72 times higher than those of the standard QTF. The MDLs were found to be 101 and 52 ppb for the round-head LiNTF and tapered LiNTF-based LITES sensors, respectively. In the future, the performance of LiNTFs might be further enhanced by optimizing the electrode coating process to reduce charge loss and adjusting the fork geometry to minimize air damping. Overall, this study provides a solid foundation for the development of high-performance LiNTF-based gas sensors in laser spectroscopy.

AUTHOR DECLARATIONS
Conflict of Interest

The authors have no conflicts to disclose.

Author Contributions

Runqiu Wang and **Guowei Han** contributed equally to this work.

Runqiu Wang: Formal analysis (equal); Investigation (lead); Software (equal); Writing – original draft (lead). **Guowei Han:** Formal analysis (equal); Methodology (equal). **Ying He:** Funding acquisition (equal); Visualization (equal). **Shunda Qiao:** Funding acquisition (equal); Visualization (equal). **Yufei Ma:** Conceptualization (lead); Funding acquisition (equal); Project administration (lead); Supervision (lead); Writing – review & editing (lead).

DATA AVAILABILITY

The data that support the findings of this study are available from the corresponding author upon reasonable request.

REFERENCES

[1] Y. Z. Liu, W. T. Cai, Y. D. Tan, T. P. Hua, C. F. Cheng, and S. M. Hu, "Trace molecular detection with wavelength-modulated cavity-enhanced two-photon absorption spectroscopy," Appl. Phys. B **131**, 99 (2025).

[2] Z. K. Zhao, W. J. Ni, C. Y. Yang, S. X. Ran, B. Z. He, R. M. Wu, P. Lu, and P. P. Shum, "Highly sensitive and miniaturized microcone-curved resonant photoacoustic cavity for trace gas detection," Photoacoustics **40**, 100650 (2024).

[3] Y. Q. Wang, J. H. Zhang, Y. C. Zheng, Y. R. Xu, J. Q. Xu, J. Jiao, Y. Su, H. F. Lü, and K. Liang, "Brillouin scattering spectrum for liquid detection and applications in oceanography," Opto-Electron. Adv. **6**, 220016 (2023).

[4] H. Y. Sun, Y. He, S. D. Qiao, C. Zhang, and Y. F. Ma, "Highly sensitive H$_2$S-LITES sensor with 80 m fiber-coupled multi-pass cell based on optical path multiplexing technology," Photoacoustics **42**, 100699 (2025).

[5] Z. X. Wu, Q. L. Ding, H. Wang, J. D. Ye, Y. B. Luo, J. H. Yu, R. Z. Zhan, H. Zhang, K. Tao, C. Liu, and J. Wu, "A humidity-resistant, sensitive, and stretchable hydrogel-based oxygen sensor for wireless health and environmental monitoring," Adv. Funct. Mater. **34**, 2308260 (2024).

[6] K. D. Benkstein, P. H. Rogers, C. B. Montgomery, C. Jin, B. Raman, and S. Semancik, "Analytical capabilities of chemiresistive microsensor arrays in a simulated Martian atmosphere," Sens. Actuator B **197**, 280–291 (2014).

[7] Q. D. Zhang, T. T. Zhang, Y. B. Wei, and T. Y. Liu, "Highly sensitive and reliable optical fiber TDLAS gas detection system for methane *in situ* monitoring in near space," Appl. Opt. **62**, 4409–4414 (2023).

[8] H. Y. Sun, Y. He, S. D. Qiao, Y. H. Liu, and Y. F. Ma, "Highly sensitive and real-simultaneous CH$_4$/C$_2$H$_2$ dual-gas LITES sensor based on Lissajous pattern multi-pass cell," Opto-Electron. Sci. **3**, 240013 (2024).

[9] H. H. Liu, D. J. J. Hu, Q. Z. Sun, L. Wei, K. W. Li, C. R. Liao, B. Z. Li, C. Zhao, X. Y. Dong, Y. H. Tang, Y. H. Xiao, G. Keiser, and P. P. Shum, "Specialty optical fibers for advanced sensing applications," Opto-Electron. Sci. **2**, 220025 (2023).

[10] J. Ma, E. B. Fan, H. J. Liu, Y. Zhang, C. Mai, X. Li, W. Jin, and B. O. Guan, "Microscale fiber photoacoustic spectroscopy for *in situ* and real-time trace gas sensing," Adv. Photonics **6**, 066008 (2024).

[11] Q. X. Nie, Y. B. Peng, Q. H. Chen, N. W. Liu, Z. Wang, C. Wang, and W. Ren, "Agile cavity ringdown spectroscopy enabled by moderate optical feedback to a quantum cascade laser," Opto-Electron. Adv. **7**, 240077 (2024).

[12] Y. H. Liu, S. D. Qiao, C. Fang, Y. He, H. Y. Sun, J. Liu, and Y. F. Ma, "A highly sensitive LITES sensor based on a multi-pass cell with dense spot pattern and a novel quartz tuning fork with low frequency," Opto-Electron. Adv. **7**, 230230 (2024).

[13] B. T. Fu, R. H. Gao, N. Yao, H. S. Zhang, C. T. Li, J. T. Lin, M. Wang, L. L. Qiao, and Y. Cheng, "Soliton microcomb generation by cavity polygon modes," Opto-Electron. Adv. **7**, 240061 (2024).

[14] Y. He, S. D. Qiao, T. E. Lang, C. Zhang, H. Qi, W. X. Huang, and Y. F. Ma, "Optical component-free dual-gas quartz-enhanced photoacoustic spectroscopy sensor based on highly integrated interband cascade lasers," ACS Sens. **10**, 5238–5244 (2025).

[15] S. D. Qiao, Y. He, H. Y. Sun, P. Patimisco, A. Sampaolo, V. Spagnolo, and Y. F. Ma, "Ultra-highly sensitive dual gases detection based on photoacoustic spectroscopy by exploiting a long-wave, high-power, wide-tunable, single-longitudinal-mode solid-state laser," Light Sci. Appl. **13**, 100 (2024).

[16] T. G. Li, P. C. Zhao, P. Wang, K. V. Krishnaiah, W. Jin, and A. P. Zhang, "Miniature optical fiber photoacoustic spectroscopy gas sensor based on a 3D micro-printed planar-spiral spring optomechanical resonator," Photoacoustics **40**, 100657 (2024).

[17] R. Wang, X. Guan, S. Qiao, Q. Jia, Y. He, S. Wang, and Y. Ma, "Ultrahigh sensitive LITES sensor based on a trilayer ultrathin perfect absorber coated T-head quartz tuning fork," Laser Photonics Rev. **19**, 2402107 (2025).

[18] L. J. Fu, P. Lu, Y. F. Pan, Y. Zhong, C. T. Sima, Q. Wu, J. S. Zhang, L. Z. Cui, and D. M. Liu, "All-optical non-resonant photoacoustic spectroscopy for multi-component gas detection based on aseismic photoacoustic cell," Photoacoustics **34**, 100571 (2023).

[19] L. Dong, A. A. Kosterev, D. Thomazy, and F. K. Tittel, "QEPAS spectrophones: Design, optimization, and performance," Appl. Phys. B **100**, 627–635 (2010).

[20] C. Z. Sang, C. Zhang, R. Q. Wang, S. D. Qiao, Y. He, and Y. F. Ma, "Tapered acoustic resonator-based quartz-enhanced photoacoustic spectroscopy," Opt. Lett. **50**, 4646–4649 (2025).

[21] A. Zifarelli, G. Negro, L. A. Mongelli, A. Sampaolo, E. Ranieri, L. Dong, H. P. Wu, P. Patimisco, G. Gonnella, and V. Spagnolo, "Effect of gas turbulence in quartz-enhanced photoacoustic spectroscopy: A comprehensive flow field analysis," Photoacoustics **38**, 100625 (2024).

[22] Y. F. Ma, Y. He, Y. Tong, X. Yu, and F. K. Tittel, "Quartz-tuning-fork enhanced photothermal spectroscopy for ultra-high sensitive trace gas detection," Opt. Express **26**, 32103–32110 (2018).

[23] S. D. Russo, A. Zifarelli, P. Patimisco, A. Sampaolo, T. T. Wei, H. P. Wu, L. Dong, and V. Spagnolo, "Light-induced thermo-elastic effect in quartz tuning forks exploited as a photodetector in gas absorption spectroscopy," Opt. Express **28**, 19074–19084 (2020).

[24] L. E. Hu, C. T. Zheng, M. H. Zhang, K. Y. Zheng, J. Zheng, Z. W. Song, X. Y. Li, Y. Zhang, Y. D. Wang, and F. K. Tittel, "Long-distance *in-situ* methane detection using near-infrared light-induced thermo-elastic spectroscopy," Photoacoustics **21**, 100230 (2021).

[25] X. Chen, R. Y. Qu, H. Liu, L. Yao, Z. Y. Xu, M. Hu, W. Wang, and R. F. Kan, "MXene-coated quartz tuning fork for sensitive light-induced thermoelastic spectroscopy," Opt. Express **33**, 1394–1405 (2025).

[26] B. Sun, P. Patimisco, A. Sampaolo, A. Zifarelli, V. Spagnolo, H. P. Wu, and L. Dong, "Light-induced thermoelastic sensor for ppb-level H$_2$S detection in a SF$_6$ gas matrices exploiting a mini-multi-pass cell and quartz tuning fork photodetector," Photoacoustics **33**, 100553 (2023).

[27] H. Liu, X. Chen, M. Hu, H. R. Wang, L. Yao, Z. Y. Xu, G. S. Ma, Q. Wang, and R. F. Kan, "In situ high-precision measurement of deep-sea dissolved methane by quartz-enhanced photoacoustic and light-induced thermoelastic spectroscopy," Anal. Chem. **96**, 12846–12853 (2024).

[28] A. Zifarelli, A. Sampaolo, P. Patimisco, M. Giglio, M. Gonzalez, H. P. Wu, L. Dong, and V. Spagnolo, "Methane and ethane detection from natural gas level down to trace concentrations using a compact mid-IR LITES sensor based on univariate calibration," Photoacoustics **29**, 100448 (2023).

[29] H. Y. Sun, Y. H. Liu, Y. He, S. D. Qiao, and Y. F. Ma, "Highly sensitive CH$_4$/C$_2$H$_2$ dual-gas light-induced thermoelastic spectroscopy sensor based on a dual-path multiring multipass cell and a circle-head quartz tuning fork," ACS Sens. **10**, 4717–4724 (2025).

[30] J. L. Dai, C. Y. Wang, P. H. Liu, L. Huang, Y. F. Li, C. G. Lou, and Y. F. Ma, "Sensitive light-induced thermoelastic spectroscopy-based oxygen sensor with a Perovskite-modified quartz tuning fork," IEEE Sens. J. **23**, 22380–22388 (2023).

[31] Y. F. Ma, X. R. Sun, H. Y. Sun, Y. He, and S. D. Qiao, "An ultra-highly sensitive LITES sensor based on multi-pass cell with ultra-dense spot pattern designed by multi-objective algorithm," PhotoniX **6**, 26 (2025).

[32] Z. J. Shang, H. P. Wu, G. Wang, R. Y. Cui, B. Li, T. Gong, G. Q. Guo, X. B. Qiu, C. L. Li, and L. Dong, "Robust and compact light-induced thermoelastic sensor for atmospheric methane detection based on a vacuum-sealed subminiature tuning fork," Photoacoustics **42**, 100691 (2025).

[33] H. Y. Sun, S. D. Qiao, Y. He, X. R. Sun, and Y. F. Ma, "Parts-per-quadrillion level gas molecule detection: CO-LITES sensing," Light Sci. Appl. **14**, 180 (2025).

[34] S. Angstenberger, M. Floess, L. Schmid, P. Ruchka, T. Steinle, and H. Giessen, "Coherent control in quartz-enhanced photoacoustics: Fingerprinting a trace gas at ppm-level within seconds," Optica **12**, 1–4 (2025).

[35] Z. T. Lang, S. D. Qiao, and Y. F. Ma, "Fabry–Perot-based phase demodulation of heterodyne light-induced thermoelastic spectroscopy," Light Adv. Manuf. **4**, 23 (2023).

[36] A. F. P. Cantatore, G. Menduni, A. Zifarelli, P. Patimisco, M. Giglio, M. Gonzalez, H. R. Seren, P. Luo, V. Spagnolo, and A. Sampaolo, "Methane, ethane, and propane detection using a quartz-enhanced photoacoustic sensor for natural gas composition analysis," Energy Fuels **39**, 638–646 (2025).

[37] D. Zhang, H. Zhang, H. Fan, M. Hu, H. Wang, J. Zhou, J. Lv, J. Liang, and Q. Wang, "Cavity-enhanced light-induced thermoelastic spectroscopy for trace-gas sensing," Opt. Express **32**, 33618–33627 (2024).

[38] Q. Wu, H. Lv, L. Lin, H. Wu, M. Giglio, W. Zhu, Y. Zhong, A. Sampaolo, P. Patimisco, L. Dong, V. Spagnolo, J. Yu, and H. Zheng, "Clamp-type quartz tuning fork enhanced photoacoustic spectroscopy," Opt. Lett. **47**, 4556–4559 (2022).

[39] R. Q. Wang, S. D. Qiao, Y. He, and Y. F. Ma, "Highly sensitive laser spectroscopy sensing based on a novel four-prong quartz tuning fork," Opto-Electron. Adv. **8**, 240275 (2025).

[40] Y. F. Ma, S. D. Qiao, R. Q. Wang, Y. He, C. Fang, and T. T. Liang, "A novel tapered quartz tuning fork-based laser spectroscopy sensing," Appl. Phys. Rev. **11**, 041412 (2024).

[41] P. Patimisco, A. Sampaolo, M. Giglio, S. Dello Russo, V. Mackowiak, H. Rossmadl, A. Cable, F. K. Tittel, and V. Spagnolo, "Tuning forks with optimized geometries for quartz-enhanced photoacoustic spectroscopy," Opt. Express **27**, 1401–1415 (2019).

[42] C. Fang, T. T. Liang, S. D. Qiao, Y. He, Z. C. Shen, and Y. F. Ma, "Quartz-enhanced photoacoustic spectroscopy sensing using trapezoidal- and round-head quartz tuning forks," Opt. Lett. **49**, 770–773 (2024).

[43] L. H. Wang, H. H. Lv, Y. H. Zhao, C. L. Wang, H. J. Luo, H. Y. Lin, J. B. Xie, W. G. Zhu, Y. C. Zhong, B. Liu, J. H. Yu, and H. D. Zheng, "Sub-ppb level HCN photoacoustic sensor employing dual-tube resonator enhanced clamp-type tuning fork and U-net neural network noise filter," Photoacoustics **38**, 100629 (2024).

[44] P. Patimisco, A. Sampaolo, M. Giglio, V. Mackowiak, H. Rossmadl, B. Gross, A. Cable, F. K. Tittel, and V. Spagnolo, "Octupole electrode pattern for tuning forks vibrating at the first overtone mode in quartz-enhanced photoacoustic spectroscopy," Opt. Lett. **43**, 1854–1857 (2018).

[45] A. Sampaolo, P. Patimisco, L. Dong, A. Geras, G. Scamarcio, T. Starecki, F. K. Tittel, and V. Spagnolo, "Quartz-enhanced photoacoustic spectroscopy exploiting tuning fork overtone modes," Appl. Phys. Lett. **107**, 231102 (2015).

[46] F. J. Giessibl, F. Pielmeier, T. Eguchi, T. An, and Y. Hasegawa, "Comparison of force sensors for atomic force microscopy based on quartz tuning forks and length-extensional resonators," Phys. Rev. B **84**, 125409 (2011).

[47] M. Toda, M. Thompson, A. Sirven, and C. Nordin, "The influence of oil density and viscosity on the behavior of a lithium niobate tuning fork cantilever," in *IEEE International Ultrasonics Symposium (IUS)* (IEEE, 2012), pp. 1–4.

[48] W. S. Weng, "Electromechanical coupling coefficients for some modes of vibration of lithium niobate single crystal," Acta Acust. **10**, 180–189 (1985).

[49] K. F. Chen, Y. Z. Zhu, Z. H. Liu, and D. F. Xue, "State of the art in crystallization of LiNbO$_3$ and their applications," Molecules **26**, 7044 (2021).

[50] M. A. Fakhri, H. D. Jabbar, F. H. Alsultany, E. T. Salim, and U. Hashim, "Lithium niobate-based sensors: A review," AIP Conf. Proc. **2660**, 020124 (2022).

[51] Y. Wang and Y. J. Jiang, "Crystal orientation dependence of piezoelectric properties in LiNbO$_3$ and LiTaO$_3$," Opt. Mater. **23**, 403–408 (2003).

[52] K. Ono, M. Yachi, and N. Wakatsuki, "H-type single crystal piezoelectric gyroscope of an oppositely polarized LiNbO$_3$ plate," Jpn. J. Appl. Phys., Part 1 **40**, 3699 (2001).

[53] Y. Liu, R. Difoggio, K. Sanderlin, L. Perez, and J. S. Zhao, "Measurement of density and viscosity of dodecane and decane with a piezoelectric tuning fork over 298–448 K and 0.1–137.9 MPa," Sens. Actuator A **167**, 347–353 (2011).

[54] M. Tang, D. H. Chen, M. Zhang, F. Jiang, and Y. Wang, "Optimized design of lithium niobate tuning forks for the measurement of fluid characteristic parameters," Micromachines **14**, 2138 (2023).

[55] A. V. Turutin, J. V. Vidal, I. V. Kubasov, A. M. Kislyuk, D. A. Kiselev, M. D. Malinkovich, Y. N. Parkhomenko, S. P. Kobeleva, A. L. Kholkin, and N. A. Sobolev, "Highly sensitive magnetic field sensor based on a metglas/bidomain lithium niobate composite shaped in form of a tuning fork," J. Magn. Magn. Mater. **486**, 165209 (2019).

[56] A. F. P. Cantatore, G. Menduni, A. Zifarelli, P. Patimisco, M. Gonzalez, H. R. Seren, V. Spagnolo, and A. Sampaolo, "Lithium niobate-enhanced photoacoustic spectroscopy," Photoacoustics **35**, 100577 (2024).